Final Research Report:

Electronic and spin properties of one-dimensional semiconductor systems

Researcher: Sébastien Faniel
Advisor: Sorin Melinte

1. Initial objectives

The purpose of our project was to study the transport properties of narrow constrictions called "quantum point contacts" built from III-V heterostructures. Recent experiments [1] have suggested that quantum point contacts subjected to a lateral electric field, between their side gates, exhibit conductance plateaus in e^2/h rather than $2e^2/h$. This was interpreted as a splitting of the spin subbands within the quantum point contact, stemming from the Rashba spin-orbit interaction induced by the lateral electric field between the side gates. In such configuration, the quantum point contacts could possibly be used as spin polarizers or spin detectors in a spin device. In this context, the purpose of our studies was to measure the e^2/h quantification in quantum point contacts made from materials with large spin-orbit interaction, and to image the electron spin transport by means of a scanning gate microscope in a specific device.

Another aspect of the research project was to investigate the transport properties of Ge/SiGe core-shell nanowires [2]. The one-dimensional carrier system confined in these nanowires is expected to exhibit a long spin relaxation time of interest for the fields of Quantum Computing and Spintronics. The aim of the project is to investigate the electronic and spin properties of single nanowires and nanowires' quantum dots through low temperature magnetostransport measurements, as well as Scanning Tunneling Microscopy and Scanning Tunneling Spectroscopy.

2. Scientific results.

Spin-orbit interaction in III-V quantum point contacts

The material chosen for these investigations were InGaAs/InAlAs heterostructures. These systems present a large Rashba spin-orbit interaction and have rather good mobilities. The latter ensures that the transport is ballistic at low temperature. The heterostructures were obtained from our collaboration with the group of Prof X. Wallart from IEMN, Lille.

After developing the fabrication process in the UCL WinFab cleanrooms, we have built several samples from different heterostructures (see Fig.1(a)). Only one wafer provided usable devices. The samples made from the other heterostructures encountered side gate leaks problems.

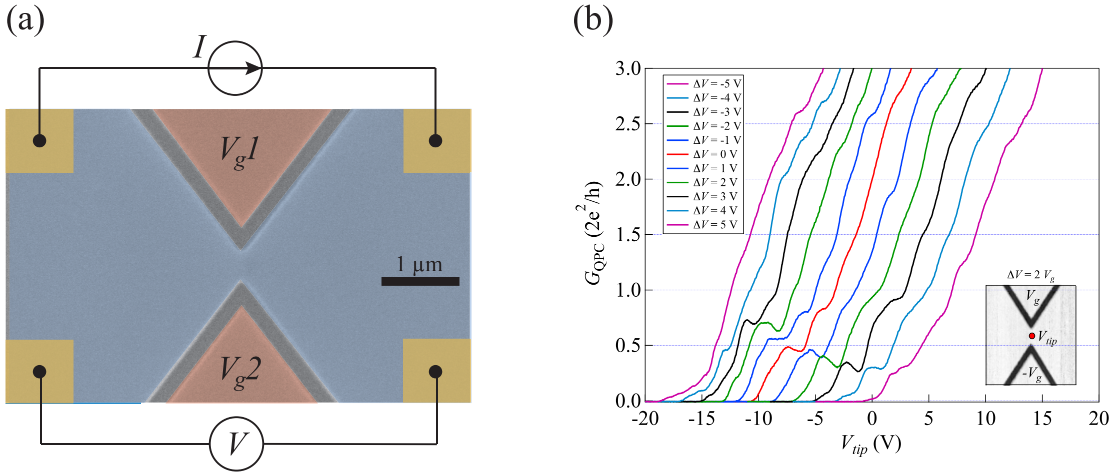

Figure 1: (a) SEM picture of an InGaAs quantum point contact and schematic illustration of the measurements setup. The blue area corresponds to the zone where the electrons are confined, while the red areas are the side gates used to apply a lateral electric field to the constriction. (b) Conductance of a quantum point contact as a function of the SGM tip voltage, while the tip is located just above the device. Traces are plotted for various values of the lateral electric field.

The low temperature measurements (4K) of our quantum point contacts show series of plateaus while the constriction is pinched off by means scanning gate tip voltage (see Fig.1 (b)). When a lateral electric field is applied to the quantum point contacts using side gates, we clearly measure a shift of the value of the conductance plateaus. However, the results' analysis is particularly difficult since the conductance plateaus do not always appear at multiple of e^2/h or $2e^2/h$. We attribute these plateaus to the presence of impurities and defects in the constriction, which generates resonance in the QPC's conductance [3], leading to peak/plateau in the g vs V_g traces. Therefore, we cannot unambiguously assign the effect of the lateral electric field to a splitting of the spin subbands within the quantum point contact for the current samples. Heterostructures with higher mobility where clean constrictions can be patterned are definitely required to highlight the effect of spin-orbit interaction on the spin spitting in quantum point contacts.

To go on with these studies, we plan to fabricate new samples using InGaAs/InAlAs heterostructures with higher mobilities, as well as heterostructures made from different materials. We have actually already started to develop the fabrication process for InAs/GaSb systems. Most fabrications steps are now under controlled, except the etching process of the quantum point contact that requires a dry plasma etching (BCl_3). Since the experimental setup for such a dry etching of InAs/GaSb is not available in the WinFab facilities, we are planning to perform the development of this fabrication step in collaboration with the group of Prof. T. Koga from Hokkaido University.

III-V quantum point contacts in a strong magnetic field

Another aspect of the electronic transport in our quantum point contacts is its properties at high magnetic fields. While they were initially not planed, these measurements provided very surprising and interesting results, and became our main research subject. Our disordered quantum point contacts were found to behave as quantum Hall interferometers [4] in the quantum Hall regime. The analysis of these data is now in progress, in collaboration with Prof. Bernd Rosenow from Leipzig University.

When subjected to a strong magnetic field, a two-dimensional electron gas (2DEG) enters the quantum Hall regime. In a quantum Hall state, the electric transport in the 2DEG occurs via one-dimensional channels along the edge of the system. Edge states propagating the electric current in opposite directions are located on opposite sides of the sample, giving rise to a dissipationless transport. Confining the 2DEG to a mesoscopic sample, brings these counter-propagating edge states into close proximity allowing carriers to tunnel between opposite sides of the device, and consequently, leads to dissipation [5]. Taking advantage of this edge states interaction, quantum Hall interferometers, like antidots in quantum point contacts (QPC) [6] or Fabry-Pérot interferometers in open quantum dots [7], have been realized. When the magnetic field B or a gate voltage, controlling the interferometers' size, is swept, the resistance of such devices exhibits oscillations whose detailed analysis shed light on the nature of the specific carriers populating the investigated quantum Hall states. In particular, quantum Hall interferometers have been predicted to be promising candidates to reveal non-abelian statistics in the quantum Hall regime [8]. While the demonstration of non-abelian statistics remains a challenge, experimental studies in quantum Hall interferometers, performed both in the integer and fractional quantum Hall regime, have provided a measure of the carriers' charge [6] and have identified different transport regimes, namely, the Coulomb dominated and Aharonov-Bohm dominated regimes [9].

Resistance oscillations in large quantum Hall interferometers, where Coulomb interaction is negligible, have been shown to stem from Aharonov-Bohm interferences. In smaller interferometers with substantial Coulomb interaction, on the other hand, they can be associated with Coulomb blockade transport. Whereas both transport regimes give rise to similar resistance oscillations, careful studies [9] have identified specific signatures for each regime, including different B period dependence on the number of occupied Landau levels, different gate voltage period dependence as a function of B, and different slope sign for the resistance stripes observed in the B-gate voltage plots. In addition, quantum Hall interferometers spectroscopies performed as a function of the excitation voltage and B have been found to exhibit a checkerboard pattern in the Aharonov-Bohm dominated regime and Coulomb diamonds in the Coulomb dominated regime.

Our sample is built from an $In_{0.7}Ga_{0.3}As/In_{0.52}Al_{0.48}As$ quantum well grown by molecular beam epitaxy on an InP substrate. The electrons are confined to a 15 nm thick quantum well buried 25 nm below the surface, producing a 2DEG with a bare electronic density N_S = 5.7 x 10^{15} m^{-2} and a mobility μ = 5.3 m^2/Vs. The 2DEG was electrically contacted by means of Ge/Au ohmic contacts. The hallbar and the QPC were patterned using electron beam lithography and wet etching. The QPC consists of two narrow trenches defining a constriction of 350 nm (see Fig. 2(a)). The 2DEG areas beyond the etched trenches of the QPC were used as side gates in order to control the opening of the constriction. Transport measurements were performed in a dilution refrigerator ($T \sim$ 100 mK) with B applied perpendicular to the plane of the 2DEG. The sample's resistance $R = \mathrm{d}V/\mathrm{d}I$ was measured using a standard ac lock-in techniques with an excitation current of 2 nA, and frequencies between 8 Hz and 90 Hz. The dilution refrigerator was also equipped with an atomic force microscope whose metallic tip could acts as a local gate. Using this specific tool, we acquired SGM images of the device by recording its resistance while the tip biased at a voltage V_{tip} was scanning the sample's surface at a distance of ~ 60 nm. In addition, two types of spectroscopies were obtained. For this purpose, a dc electric current I was added to the lock-in signal, and the QPC's differential resistance $R = \left.\frac{dV}{dI}\right|_I$ was recorded as a function of: first, I and B; or second, I and V_{tip}, keeping the tip at a fixed position next to the QPC.

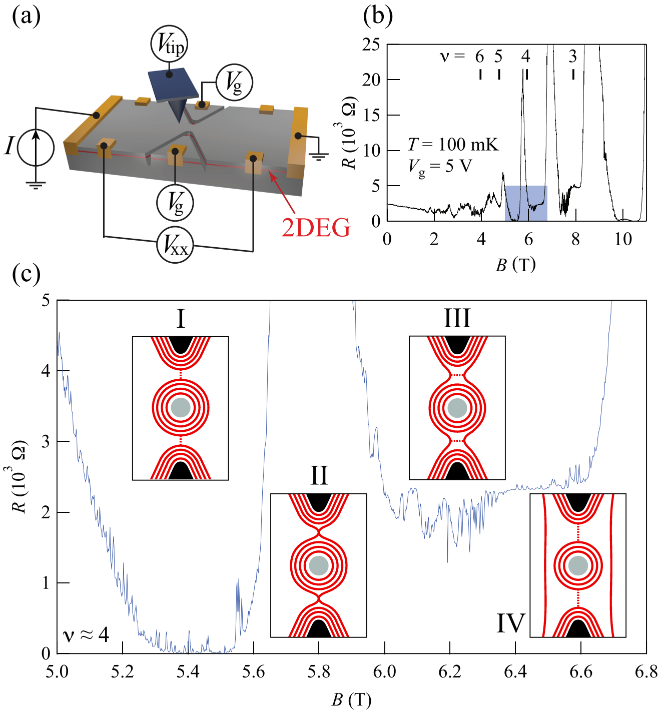

Figure 2: (a) Schematic representation of the sample and measurement layout. (b) Magnetoresistance of the QPC at $T = 100$ mK and $V_g = 5$ V. (c) Magnified view of the QPC's magnetoresistance around $\nu = 4$ (shaded area in (b)). The insets to (c) show the edge states configuration in the QPC for various B-ranges. The red plain lines represent the edge states while the red dashed lines are the tunneling paths between the edge states.

In Fig. 2(b), we first present the magnetoresistance of the QPC at 100 mK for a side gates' voltage $V_g = 5$ V. The trace shows large Shubnikov-de Haas oscillations stemming from the magnetic depopulation of the Landau Levels in the 2DEG, together with series of smaller oscillations in the vicinity integer filling factor ν. Similar resistance oscillations around integer quantum Hall states have been reported in QPCs and where attributed to the interaction between the counter-propagating quantum Hall edge states in the mesoscopic system. Two different models were proposed to explain the apparition of such conductance oscillations in QPCs: the first one is an interferometer resulting from the formation of two tunnelling paths connecting counter-propagating edge states on each sides of the potential saddle point, while the second one consists in the presence of a small quantum Hall island (QHI) next to the QPC due to potential inhomogeneities. Around $\nu = 4$, the QPC's magnetoresistance exhibits four different regimes as B is raised (see Fig. 2(c)). First, in the lowest B region of the $\nu = 4$ quantum Hall state ($5.2 \text{ T} \leq B \leq 5.6$ T), the QPC's resistance shows series of narrow peaks superimposed on a plateau at zero. Second, when B is raised ($5.6 \text{ T} \leq B \leq 6$ T), a large magnetoresistance peak is observed. Third, when B is further increased, the QPC's magnetoresistance exhibits dips below a plateau value at ~ 2300 Ω. And fourth, in the higher B part of the $\nu = 4$ plateau ($6.4 \text{ T} \leq B \leq 6.7$ T), magnetoresistance peaks are observed above the plateau value. This magnetoresistance sequence is consistent with the formation of small disordered-induced QHI in the QPC, as previously reported in similar disordered nanostructures [10]. While B is raised, one of the edge states is progressively depopulated in the constriction, giving rise to different edge state configurations in the QPC/QHI system, as illustrated in the inset to Fig. 2(c). Each configuration is linked to an observed magnetoresistance regime. Configuration I corresponds to $5.2 \text{ T} \leq B \leq 5.6$ T. The four edge states are transmitted through the QPC leading to a resistance plateau at 0. A potential hill next to the QPC, represented as a grey circle, is surrounded by the edge states and forms a QHI. Electron tunnelling between the counter-propagating edge states occurs via the QHI and leads to electron backscattering, which, in turn, produces resistance peak. When B increases, the highest energy Landau level overlaps with the Fermi energy in the QPC as depicted in configuration II. In that case, electrons' backscattering between the counter-propagating edge states on both sides of the QPC is strongly enhanced and a large resistance peak is observed. When B is further raised, the highest energy Landau level is raised above the Fermi in the QPC and the corresponding edge state is reflected. The number of edge states in the bulk, N = 4, and in the QPC, $N^* = 3$, are then different and the QPC's background resistance shows the expected plateau at a value $R = 2151\ \Omega$, obtained from

$$R = \frac{h}{e^2}\left(\frac{1}{N^*} - \frac{1}{N}\right)$$

where e is the electron charge and h is the Planck constant. Right after the depopulation of the highest energy Landau Level in the QPC ($6\ \mathrm{T} \leq B \leq 6.4\ \mathrm{T}$), the corresponding edge states wraps around the QHI as show in configuration III. Two tunnelling paths appear on both sides of the QHI, forming an interferometer that produces resistance's oscillations. Since the electron tunnelling in the interferometer leads to an enhancement of the electron forward scattering through the QPC, these oscillations reduces the QPC's resistance below the plateau value. We also note that the observed oscillations are not periodic, indicating that several QHIs may be active at the same time. When $B \geq 6.4$ T, the reflected edge states is completely expelled from the QPC and do not contribute to the transport anymore. This is illustrated in configuration IV. At these specific B's, the electron backscattering occurs through the central QHI and gives rise to peaks above the magnetoresistance plateau.

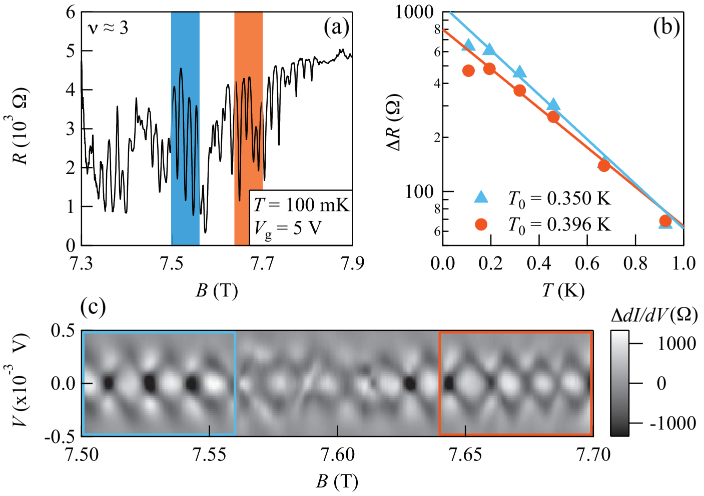

Figure 3 : (a) Magnetoresistance of the QPC around ν = 3 for T = 100 mK and V_g = 5 V. (b) Temperature dependence of the amplitude of the magnetoresistance oscillations presented in (a). The red circles and blue triangles correspond to the red and blue shaded areas in (a), respectively. The plain lines are fits to the data using $\Delta R = A\, exp\left(-\frac{T}{T_0}\right)$. (c) Differential resistance dV/dI of the QPC as a function of B and the dc bias voltage V. The red and blue boxes correspond to the red and blue shaded area of panel (a), respectively. A slowly varying background was subtracted from the data.

We now focus on the data obtained in the vicinity the $\nu = 3$ quantum Hall state. Figure 3 (a) shows the resistance of the QPC as a function of B that exhibits periodic oscillations below a plateau at ~ 4300 Ω. This resistance plateau corresponds to the reflexion of one of the edge states in the QPC (N = 3, $N^* = 2$). The edge states configuration is then similar to configuration III in Fig. 2(c): two edge states are transmitted through the QPC, while the third one is reflected but wraps around the QHI, forming an interferometer. The periodicity of the oscillations with a frequency of ~ 63 T^{-1} ensures that only one QHI is active. The magnetoresistance oscillations' period in a quantum Hall interferometer is equal to Φ_0/A for the Aharonov-Bohm dominated regime, while for the Coulomb blockade regime it depends on the number of transmitted edge states in the QPC, N^*, and is given by Φ_0/AN^*. Here, Φ_0 is the flux quantum and A is the area of the quantum Hall interferometer. Assuming a circular QHI, we obtain a diameter d_a of ~ 400 nm and ~ 575 nm for the Coulomb-dominated and Aharonov-Bohm-dominated regimes, respectively. In Fig. 3(c), we plot the differential resistance of the QPC near the $\nu = 3$ quantum Hall state as a function of the dc excitation voltage V and B. This provides spectroscopy data of the QHI that show Coulomb diamonds next to the resistance plateau (7.5 T $\leq B \leq$ 7.56 T) and a checkerboard pattern at lower B's (7.64 T $\leq B \leq$ 7.7 T). Figure 3(b) presents the temperature dependence of the amplitude of the magnetoresistance oscillations in these two regimes. Both exhibit an exponential dependence of the form, $\Delta R = A\, exp\left(-\frac{T}{T_0}\right)$, where A is a constant and T_0 is related to an effective charging energy. We obtain T_0 = 0.350 K and 0.396 K for the checkerboard and diamonds regime, respectively. Given that $T_0 = \frac{\Delta E_{EX}}{k_B} = 2\hbar v_a/(k_B d_a)$, for coherent quantum Hall interferometers, we obtain an edge state velocity v_a equals to 9.165 x10^3 m/s and 10.369 x 10^3 m/s for the checkerboard and diamonds regime, respectively, if we assume d_a = 400 nm.

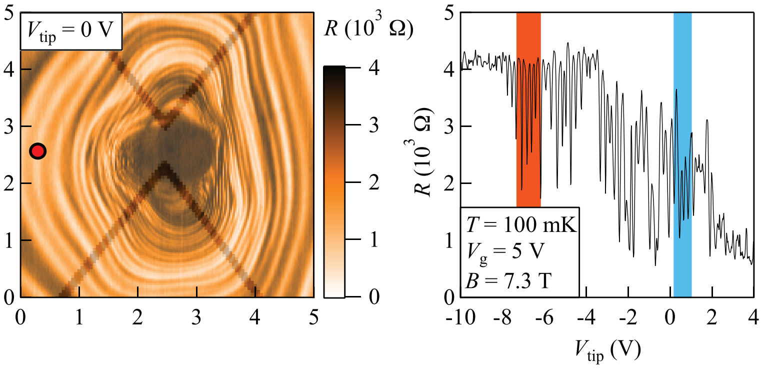

Figure 4 : Left panel: SGM image of the QPC with V_{tip} = 0 V for B = 7.3 T, T = 100 mK, and V_g = 5 V. A topography image of the QPC is shown in transparency on top of the SGM image. Right panel: Resistance of the QPC as a function of V_{tip}. The tip location for this trace is shown by the red dot on the left panel.

Similar data can be obtained as a function of the SGM voltage tip. In the left panel of Fig. 4, we present a SGM image of our QPC at B = 7.3 T and T = 100 mK, for a tip voltage V_{tip} = 0 V. A standard AFM image of the device is shown in transparency on top of the SGM image to visualize the position the QPC. The SGM image shows concentric fringes centred on the QHI, allowing us to precisely determine its location, near the constriction. When V_{tip} is decreased to negative values, the concentric fringes moves away from the QHI, while for positive V_{tip}, the situation becomes more complicated and several QHIs can be identified on the SGM plots (not shown here). A negative V_{tip} has actually a similar effect as increasing B, while V_{tip} becomes more negative, the potential in the device is raised and the third edge state is slightly expelled from the QPC. This is illustrated in the right panel of Fig. 4 that shows R as a function of V_{tip} at B = 7.3 T and T = 100 mK. The tip location for this trace is shown by the red dot in the left panel of Fig. 4. The obtained curve is similar to the magnetoresistance plotted in Fig. 3(a): while V_{tip} is decreased, the QPC's resistance exhibits periodic oscillations and then reaches a plateau when the third edges states is completely expelled from the QPC and do not contribute to the transport anymore.

Spectroscopies of the QHI were also obtained as a function of V_{tip}. These data are shown in Fig. 5(b) and (d) that present dV/dI as a function of the dc excitation voltage V and V_{tip}, for B fixed at 7.3 T and a tip location as shown by the red dot of the left panel of Fig. 4. Here again, two different regimes are observed: close to the resistance plateau that corresponds to the reflection of one edge state, the spectroscopy shows Coulomb diamond (Fig. 5 (b)). At larger V_{tip}, the spectroscopy evolves into a checkerboard pattern.

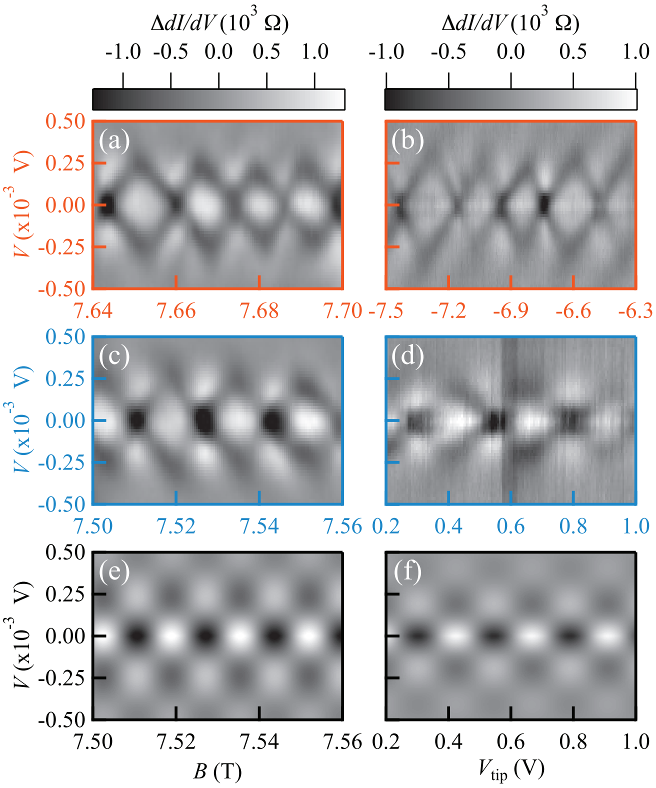

Figure 5 : Panels (a) and (c): Differential resistance dV/dI of the QPC as a function of B and the dc bias voltage V around $\nu = 3$ for $T = 100$ mK and $V_g = 5$ V. Panels (b) and (d): Differential resistance dV/dI of the QPC as a function of V_{tip} and the dc bias voltage V for $B = 7.3$ T, $T = 100$ mK and $V_g = 5$ V. The tip location is the same as in Fig. 4. The B- and V_{tip}-ranges presented here correspond to the shaded areas in Fig. 3 (a) and in the right panel of Fig. 4, respectively. Panels (e) and (f) show fits to the checkerboard spectroscopies presented in panels (c) and (d), respectively, using Eq.(1). A slowly varying background was subtracted from the data in panels (a) - (d).

We now discuss the spectroscopies obtained as a function of both B and V_{tip}. The measurements are summarized in Fig. 5 that presents the spectroscopies in the Coulomb diamonds ((a) and (b)) and checkerboard ((c) and (d)) regimes. The panels (e) and (f) are fits to the checkerboard patterns shown in panels (c) and (d), respectively, using the following equation [11]:

$$\frac{dV}{dI} = D\cos\left(2\pi\frac{V}{\Delta V}\right)\cos\left(2\pi\frac{V_{tip}}{\Delta V_{tip}} + \varphi\right)\exp\left(-2\pi\gamma\frac{V}{\Delta V}\right) \quad (1)$$

where D is the amplitude of the oscillation at zero bias, ΔV_{tip} and ΔV are the period of the oscillations as a function of V_{tip} and V, respectively, φ is a phase constant factor and γ is the V-induced dephasing factor. The fit to the V-B spectroscopy shown in panel (e) gives $\Delta V = 5.2 \times 10^{-4}$ V and $\gamma = 0.29$. As $\Delta V = 4\bar{h}v_a/(ed_a)$, we can calculate $v_a = 79 \times 10^3$ m/s, assuming $d_a =$

400 nm. From the fit to the V-V_{tip} data, we got $\Delta V = 4.31 \times 10^{-4}$ V and $\gamma = 0.345$, leading to $v_a = 65.48 \times 10^3$ m/s. We note that the values of v_a obtained here are approximately one order of magnitude larger than those extracted from the T dependence of the magnetoresistance oscillations.

The observation of a transition from Coulomb diamonds to checkerboard-like spectroscopies is rather surprising since previous results [9] indicated that the former occurs for small quantum Hall interferometers with strong electron-electron interactions, while the latter is expected for large system where electron-electron interactions are negligible. In our device, while B or V_{tip} is swept, neither the size of the system nor the strength of electron-electron interactions is tuned. However, B and V_{tip} tune the coupling of the interferometer, i.e. the tunnelling strength between the reflected edge state in configuration III of Fig. 2(c), suggesting that a transition from Coulomb diamonds to checkerboard-like spectroscopies may occur when the quantum hall interferometer goes from the strongly to weakly coupled regime.

Electronic and spin properties of semiconductor nanowires

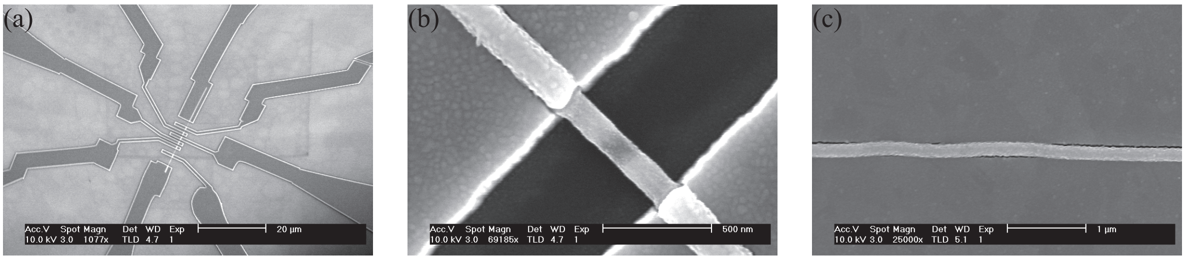

Figure 6: (a) SEM image of a Si nanowire device. Nickel Schottky contacts have been made through electron beam lithography and metallization/lift-off processes. (b) SEM image of the Si nanowire after rapid thermal annealing. The diffusion of Ni in the Si clearly be observed (bright area next to the metallic contacts). (c) SEM Image of a Si nanowire covered with Ni after annealing: the strain and metal dewetting induce a detachment of the metal from the nanowire.

We have investigated Ge/SiGe core-shell nanowires obtained via our collaboration with Prof. E. Tutuc from the University of Texas [2]. The fabrication process for nanowires-based devices is still under development. While we can now easily deposit metallic contacts, perfectly aligned, on the nanowire, we encounter difficulties to obtain ohmic contacts to the confined one-dimensional carrier system. This contact quality problem precludes any reliable electrical characterization of the nanowires at the moment. Up to now, several thermal treatments have been tested without any substantial improvement of the contact resistance.

To further understand the formation of contact to semiconductors nanowires, we have investigated the realization of Schottky contacts to Si nanowires. These contacts are made by formation of a metal silicide (Ni or Pt). Nickel contacts to silicon nanowires have been realized as shown in Fig. 6(a). The diffusion of nickel atoms in the Si nanowire and the formation of the Nickel silicide by rapid thermal annealing at 400°C for ~ 2 minutes is clearly observed in Fig. 6(b), where the bright segments of the nanowire next to metal areas is the part of the nanowire where the silicide as been formed. While the silicidation at the contact interface is realized, the devices still show bad contact performance. A more detailed study of the contact morphology has shown that dewetting of the metallic sheet from the substrate surface in responsible for the poor contact quality. The main reasons for this are the poor adhesion of the Ni layer to SiO_2 substrate and the strain induced in the nanowire during the silicidation process (see Fig. 6(c)). New approaches with additional layers of Ni and Al are now under development to overcome these problems. The Ni layer ensure a good adhesion to the substrate while the Al layer precludes the formation of void at the metal/nanowire interface. Preliminary fabrication tests provided promising results and silicon nanowires field effect transistors were successfully obtained.

[1] P. Debray et al., Nature Nanotechnology **4**, 759 (2009).
[2] E. Tutuc et al., Appl. Phys. Lett. **89**, 263101 (2006).
[3] D.I. Chang et al., Journal of the Korean Physical Society **49**, 692 (2006).
[4] B.J. van Wees et al., Phys. Rev. Lett. **62**, 2523 (1989).
[5] P.H.M. Van Loosdrecht et al., Phys. Rev. B **38**, 10162 (1988).
[6] V.J. Goldman and B. Su, Science **267**, 1010 (1995).
[7] D.T. McClure et al., Phys. Rev. Lett. **108**, 256804 (2012).
[8] A. Stern et al., Phys. Rev. B **82**, 085321 (2010).
[9] Y. Zhang et al., Phys. Rev. B **79**, 241304(R) (2009).
[10] B. Hackens et al., Nature Communications **1**, 39 (2010).
[11] D.T. McClure et al., Phys. Rev. Lett. **103**, 206806 (2009).

3. Dissemination

Publications

S. Faniel, T. Matsuura, S. Mineshige, Y. Sekine and T. Koga, "*Determination of spin-orbit coefficients in semiconductor quantums wells*". Phys Rev B **83**, 115309 (2011).

S. Mineshige, S. Kawabata, S. Faniel, J. Waugh, Y. Sekine and T. Koga, "*Semiclassical interpretation of the spin interference effect observed in square loop arrays of* $In_{0.53}Ga_{0.47}As/In_{0.52}Al_{0.48}As$ *quantum Wells*". Phys Rev B **84**, 233305 (2011).

S. Faniel, T. Matsuura, S. Mineshige, Y. Sekine and T. Koga, "*Weak localization/anti localization in a nearly symmetric* $In_{0.53}Ga_{0.47}As/In_{0.52}Al_{0.48}As$ *quantum Well*". AIP Conf. Proc. **1399**, 649 (2011).

T. Koga, S. Faniel, T. Matsuura, S. Mineshige, Y. Sekine and H. Sugiyama, "*Determination of spin-orbit coefficients and phase coherence times in InGaAs/InAlAs quantum wells*". AIP Conf. Proc. **1416**, 38 (2011).

T. Koga, T. Matsuura, S. Faniel, S. Souma, S. Mineshige, Y. Sekine and H. Sugiyama, "*Beating analysis of Shubnikov de haas oscillation in* $In_{0.53}Ga_{0.47}As$ *double quantum well toward spin filter applications*". IEICE Transactions on Electronics **E95-C**, 770 (2012).

Publications in the "Mandats de retour" framework

F. Martins, S. Faniel, B. Rosenow, M.G. Pala, H. Sellier, S. Huant, L. Desplanque, X. wallart, V. Bayot and B. Hackens, "*Scanning Gate Spectroscopy of transport across a quantum Hall Nano-Island*". New Journal of Physics, accepted for publication.

F. Martins, S. Faniel, B. Rosenow, M.G. Pala, H. Sellier, S. Huant, L. Desplanque, X. wallart, V. Bayot and B. Hackens, "*Locating an individual quantum Hall island inside a quantum ring*". AIP Conf. Proc., accepted for publication.

F. Martins, S. Faniel, B. Rosenow, H. Sellier, S. Huant, M.G. Pala, L. Desplanque, X. wallart, V. Bayot and B. Hackens, "*Coherent tunneling across a quantum point contact in the quantum Hall regime*". Submitted to Scientific Report.

S. Faniel, F. Martins, L. Desplanque, X. Wallart, S. Melinte, B. Rosenow, V. Bayot and B. Hackens, "*Transition from Coulomb Diamonds to Checkerboard-like spectroscopies in Mesoscopic Quantum Hall Islands*". In preparation.

Conferences in the "Mandats de retour" framework

S. Faniel, F. Martins, V. Bayot, B. Hackens, L. Desplanque, X. Wallart, B. Rosenow and S. Melinte "*Transition from Coulomb Diamonds to Checkerboard-like spectroscopies in Mesoscopic Quantum Hall Islands*". March Meeting of the American Physical Society 2013, Baltimore (oral presentation).

4. Summary and perspectives

The project initially aimed to investigate the electronic and spin properties of semiconductor core-shell nanowires and III-V quantum point contacts. The investigation of semiconductors nanowires has been hindered by electrical contacts problems. Several fabrication processes are now under consideration to provide better contacts to the nanowires and promising results have been obtained. In the future, I will continue these studies on semicontuctor (Si, SiGe) nanowires in collaboration with the group of Dr. Sorin Melinte, in particular with a new PhD student that has been hired recently to go on with this subject. For the second part of the project, the mobility of the III-V heterostructures we used to build the quantum point contacts were insufficient to unambiguously determine the effect of the lateral electric field on the spin-splitting in the constriction, as it was intended. Our devices were found, however, to show remarkable properties under a strong magnetic field. These surprising findings became my main research topics and several publications are in press or in preparation. In a strong magnetic field, a small disordered-induced quantum Hall island, located inside the constriction, allowed electrons to tunnel between counter-propagating edges states forming a nanoscopic quantum Hall interferometer. The most surprising aspect of the transport properties of this quantum Hall interferometer was the observation of an unexpected transition from Coulomb diamonds to checkerboard pattern in its spectroscopies, which seems to originate from the tuning of the coupling strength in the interferometer. Such quantum Hall interferometers are promising candidates to investigate quantum Hall systems with anyonic and non-abelian statistics, paving the way to topologically protected quantum computing. In this context the experimental results obtained within this last two years allowed me to obtain a new, two years, post-doctoral position within the group of Prof. Vincent Bayot at the Université catholique de Louvain. The aim of this new work will be to continue the study of quantum Hall interferometers in peculiar quantum Hall states and to develop a new characterization tool based on the combination of scanning gate microscopy and electrical noise ("shot noise") measurements.